

Magnetism of topological boundary states induced by boron substitution in graphene nanoribbons

Niklas Friedrich,^{1,*} Pedro Brandimarte,^{2,*} Jingcheng Li,¹ Shohei Saito,³ Shigehiro Yamaguchi,⁴ Iago Pozo,⁵ Diego Peña,⁵ Thomas Frederiksen,^{2,6} Aran Garcia-Lekue,^{2,6} Daniel Sánchez-Portal,^{2,7,†} and José Ignacio Pascual^{1,6,‡}

¹*CIC nanoGUNE, 20018 Donostia-San Sebastián, Spain*

²*Donostia International Physics Center (DIPC), 20018 Donostia-San Sebastián, Spain*

³*Graduate School of Science, Kyoto University, Kyoto 606-8502, Japan*

⁴*Graduate School of Science, Nagoya University, Nagoya 464-8602, Japan*

⁵*CiQUS, Centro Singular de Investigación en Química Biolóxica e Materiais Moleculares, 15705 Santiago de Compostela, Spain*

⁶*Ikerbasque, Basque Foundation for Science, Bilbao, Spain*

⁷*Centro de Física de Materiales CSIC-UPV/EHU, 20018 Donostia-San Sebastián, Spain*

(Dated: September 29, 2020)

Graphene nanoribbons (GNRs), low-dimensional platforms for carbon-based electronics, show the promising perspective to also incorporate spin polarization in their conjugated electron system. However, magnetism in GNRs is generally associated to localized states around zigzag edges, difficult to fabricate and with high reactivity. Here we demonstrate that magnetism can also be induced away from physical GNR zigzag edges through atomically precise engineering topological defects in its interior. A pair of substitutional boron atoms inserted in the carbon backbone breaks the conjugation of their topological bands and builds two spin-polarized boundary states around. The spin state was detected in electrical transport measurements through boron-substituted GNRs suspended between tip and sample of a scanning tunneling microscope. First-principle simulations find that boron pairs induce a spin 1, which is modified by tuning the spacing between pairs. Our results demonstrate a route to embed spin chains in GNRs, turning them basic elements of spintronic devices.

In spite of being a diamagnetic material, graphene can develop a special class of magnetism via the polarization of its π -electron cloud. Such π -paramagnetism is less localized than the more conventional d - or f -magnetism, and can interact over longer distances. Magnetic graphene nanostructures thus offer promising perspectives for *a la carte* engineering of interacting spin systems with applications in quantum spintronic devices [1–4]. The vision of graphene π -paramagnetism has been recently boosted by the development of on-surface synthesis (OSS) as a versatile bottom-up route. In OSS, nanoscale graphene flakes with customized shape and composition are fabricated over a metal substrate through the steered reactions between designed organic precursors [5, 6]. Solid evidence of magnetism in flakes with zigzag edges has been revealed in scanning tunneling spectroscopy experiments [7–10].

Substituting one carbon atom of the graphene lattice by heteroatoms is a potential route to induce magnetism [23, 24]. A representative case is the doping of graphene with substitutional boron atoms (Fig. 1), because it can be idealized as the removal of one electron from the conjugated bipartite lattice plus the energy upshift of a p_z state. However, boron atoms do not induce any spin imbalance around, but simply behave as a point potential [23]. A prerequisite for the emergence of π -paramagnetism is that the point defect also causes a sufficiently large rupture of the conjugated electron system, for example by completely removing lattice sites or saturating p_z orbitals [25–27], resulting in the localization of radical states.

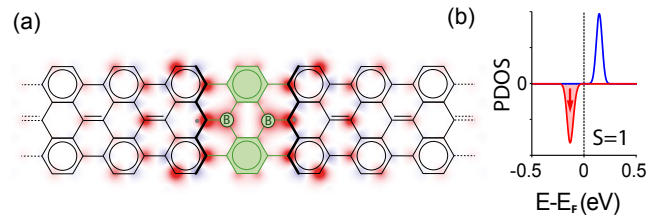


FIG. 1: (a) Lewis structure of the 2B-7AGNR shown over a colour map representing the spin polarization density map, computed by density functional theory simulations ([11]) (green represents the boron moiety). (b) Spin-resolved Projected Density of States (PDOS) over carbon atoms around the boron dimer. A net spin polarization of one kind confirms the ferromagnetic alignment of the two magnetic moments.

Here we show that inserting a pair of boron atoms in the carbon lattice of graphene nanoribbons (GNRs) enables a magnetic ground state. Density Functional Theory (DFT) simulations (Fig. 1) show that, while magnetism is completely absent around a pair of such substitutional B atoms in different sublattices of extended graphene, in a 7-carbon-wide armchair GNR (7AGNR) the boron pair builds up a net magnetic moment of $2\mu_B$ (two Bohr magnetons). The spin polarization, shown in Fig. 1(a), decays towards the pristine segments with the characteristic shape of the 7AGNR end states [28] (see Supplementary Information (SI), [11] for a comparison). In fact, the spin cloud emerges from the rupture of the conjugated system imposed by the 2B-doped ring and the two neighbouring Clar sextets (green in Fig. 1(a)).

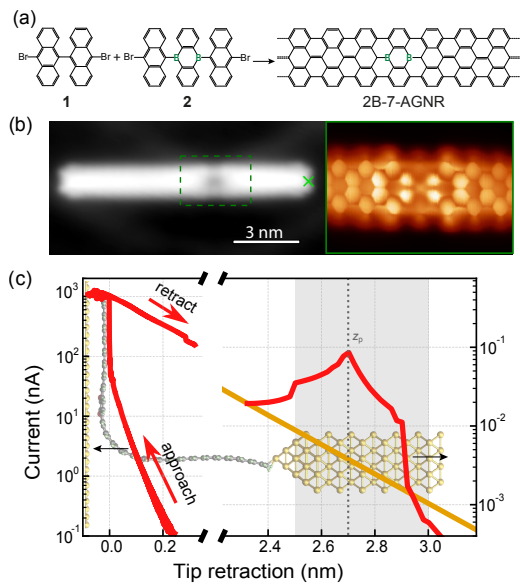


FIG. 2: (a) Organic precursors mixed in the experiments. (b) STM constant current topography image of a 2B-7AGNR ($V_b = -300$ mV, $I = 30$ pA). The green cross indicates the position from where the GNR is lifted. (right) Constant height current scan ($V_b = 2$ mV) using a CO-functionalized tip [34] of the region indicated by the dashed rectangle. (c) Tunneling current I at $V_b = 25$ mV as a function of z for a borolated (red) and a pristine (orange) GNR, for comparison. The grey region indicates where spectra in Fig. 3(b) was measured. The background shows results of atomistic simulations of a retraction stage shown in Fig. 4, for illustration.

This moiety behaves as a highly reflective barrier for valence band electrons [29, 30], thus inducing localized end states associated with the termination of the topological 7AGNR valence band [31]. This striking result offers the vision of combining band topology of nanoribbons [31–33] and heteroatoms for shaping spin textures in graphene ribbons.

In our experiments, we substitutionally inserted boron pairs (2B) inside 7GNRs (2B-7AGNRs) by adding a small fraction of 2B-doped trianthracene organic precursors (**1** in Fig. 2(a)) [29, 30, 35–38] during the OSS of 7AGNRs using precursor **2** [5] (as schematically shown in Fig. 2(a), see Methods in SI [11]). Scanning tunneling microscopy (STM) images of the fabricated ribbons (Fig. 2(b)) resolved the 2B unit as a topography depression at varying positions inside the GNR [29, 35, 36]. Tunneling spectra showed no fingerprint of magnetism around the 2B moieties due to the strong interaction between boron and metal states [30, 38], which quenches the eventual magnetic ground state. Therefore, to detect their intrinsic magnetic state the 2B moieties had to be removed from the metal substrate.

We used the STM tip to pick individual 2B-7AGNRs from one end (cross in Fig. 2(b)) and lift them off to lie free-standing between tip and sample [7, 40]. The (two-

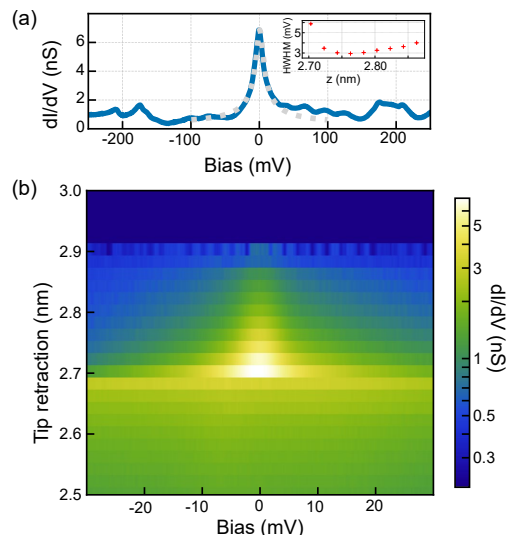


FIG. 3: (a) Spectrum over a larger bias interval, taken at $z = 2.70$ nm. The dotted grey line is a fitted Frota function [39] with $\text{HWHM} = 6.0 \pm 0.4$ mV. The fitting interval is $|V_b| < 20$ mV. The inset shows the evolution of the resonance’s HWHM as a function of z . (b) Conductance through the GNR as a function of V_b and z . The corresponding height interval is the grey region indicated in Fig. 2(c). A zero-bias, narrow resonance is observed for $2.7 \text{ nm} < z < 2.9 \text{ nm}$.

terminal) electrical transport through the suspended 2B-7AGNR was monitored during tip retraction z . At the initial stages of suspension (2B unit still on the surface), the current through the ribbon showed a weak exponential decrease with z (Fig. 2(c)), as for pristine GNRs [40]. However, at a certain retraction length z_p , the current exhibited a pronounced peak, returning afterwards to the previous exponential decay. The peak and its position z_p were reproduced for several retraction/approach cycles of the same ribbon, and appeared in all 2B-7AGNRs studied. In every case, the value of z_p correlated with the distance between the 2B site and the contacted GNR-end (see SI [11]), proving that the current peaks were caused by the detachment of a 2B moiety from the surface.

To explore the origin of the anomalous current peak, we measured differential conductance (dI/dV) spectra at positions around z_p (Fig. 3). The dI/dV plots show the emergence of a narrow zero-bias resonance in the spectra at $z_p = 2.7$ nm, which gradually decreases its amplitude with tip retraction, and disappears for $z > 2.9$ nm. The resonance remained pinned at zero bias in all the z range observed. Its narrow line width reached a maximum value of $\Gamma_{\text{HWHM}} \approx 6.0 \pm 0.4$ mV at z_p , and evolved non-monotonously with retraction z (Fig. 3(a)) until disappearing. When the tip was approached below z_p , the resonance vanished abruptly, but it was recovered by increasing z back above the $z_p = 2.7$ nm onset. From its narrow line shape and fixed zero-bias alignment, we conclude that the resonance is a manifestation of the Kondo

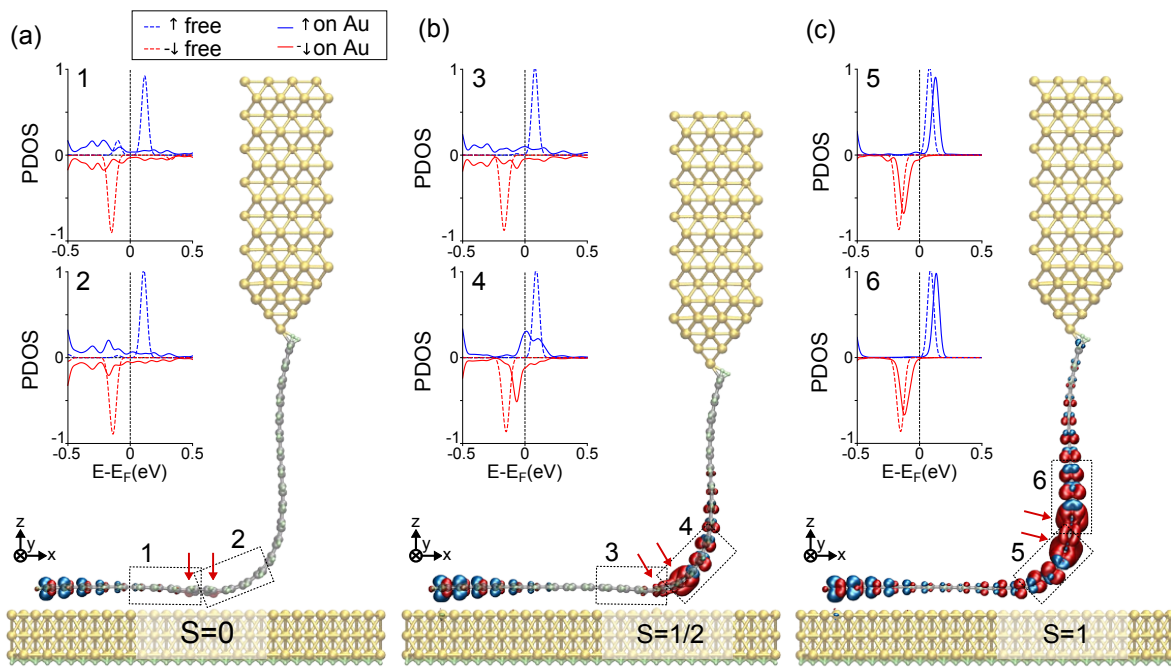


FIG. 4: (a-c) Relaxed structures of three different configurations of a 2B-7AGNR bridging a gold tip and a Au(111) surface (red arrows indicate the position of the B heteroatoms). Constant spin density isosurfaces are shown over the atomic structure ($1.7 \times 10^{-3} e/\text{\AA}^3$, spin up in blue and down in red). Insets compare spin PDOS over C atoms within the boxed regions around each boron atom for each bridge geometry (solid lines), with the corresponding one of a free 2B-7AGNR (dashed lines). The GNR zigzag termination on the surface holds a spin-polarized radical state, absent at the contacted end due to the bond formed with the tip's apex [7]. The equivalent PDOS are provided for a wider energy window in the SI.

effect [41–43]. A Kondo-derived resonance appears in dI/dV spectra when a spin polarized state weakly interacts with the conduction electrons of an underlying metal [44].

To correlate these observations with the 2B-induced spin polarization predicted in Fig. 1, we performed DFT simulations of a finite 2B-7AGNR suspended between a model gold tip and the surface of a Au(111) slab [11]. Figure 4 shows the relaxed atomic structures of the GNR-junctions before, while, and after detachment of a 2B unit, and includes the computed constant spin density isosurfaces. Before 2B-detachment from the surface ($z < z_p$, Fig. 4(a)), the intrinsic magnetism around the 2B units is quenched: the PDOS in the regions 1 and 2 around each boron atom is broad and spin unpolarized, contrasting with the clear spin polarization of free ribbons (shown as dashed plots). This is caused by the strong hybridization of the B atoms with the gold surface [30, 35], which appear 0.6 \AA closer to the surface than the carbon backbone.

The detachment of the 2B moieties from the metal surface causes the emergence of a net spin polarization, clearly reflected in their PDOS and spin density isosurfaces (Fig. 4(b,c)). At the intermediate snapshot of Fig. 4(b), only one of the two B heteroatoms is detached from the surface, and the ribbon hosts a net spin $S = 1/2$

extending towards the free-standing segment (region 4). For the fully detached 2B case (Fig. 4(c)), both regions around the two B atoms (regions 5 and 6) are spin polarized, recovering the $S = 1$ state of the isolated 2B-7AGNR (Fig. 1(b)). Based on these simulations, we interpret that the most probable origin of the experimental Kondo resonance is the intermediate configuration pictured in Fig. 4(b). There, the Kondo effect is caused by the spin $1/2$ of region 4 interacting weakly with the surface when the first boron atom is detached. Although the $S=1$ state of Fig. 4(c) could also produce a Kondo state [9], one would expect that it shows a larger extension and is accompanied by inelastic triplet-singlet side bands. Instead, the zero-bias resonance in the experiments disappears abruptly after a second kink $\sim 2 \text{ \AA}$ higher (Figs. 2c and 3b) that we associate with the cleave of the second B atom, in consistency with the B-B distance. The experimental results are thus consistent with the spin polarization around free-standing 2B moieties.

Although the Kondo signal vanishes quickly with retraction, DFT finds that the $S = 1$ state of the free ribbon remains, and is clearly favored over an anti-parallel alignment by $\sim 14 \text{ meV}$ per isolated 2B pair. The presence of a triplet state is striking; the two spin clouds at each side of the 2B center extend symmetrically over opposite sub-lattices of the 7AGNR, what usually favors an

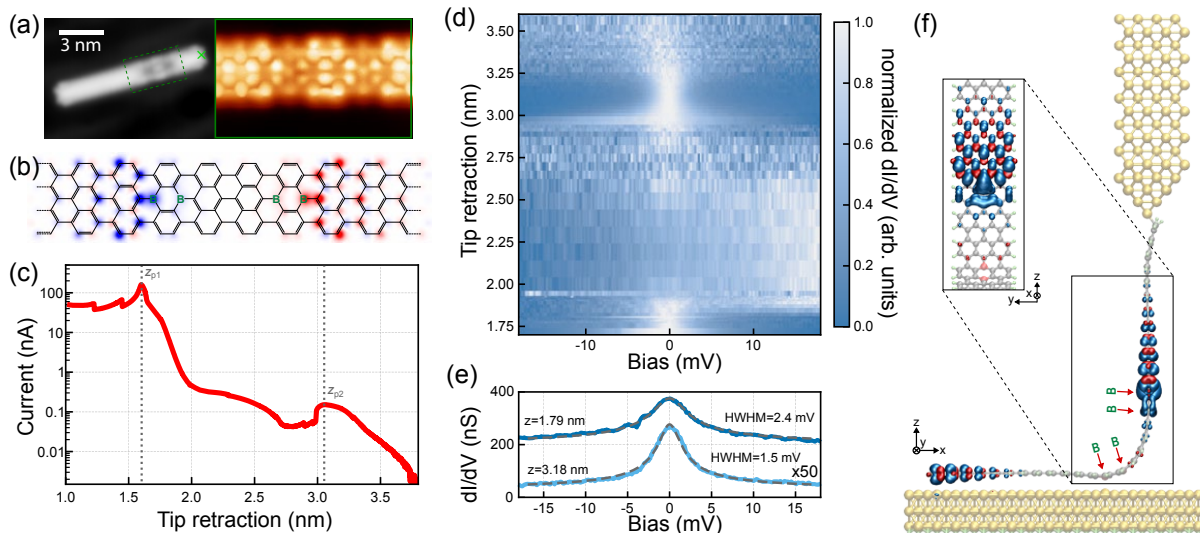


FIG. 5: (a) (Left) Constant current STM image of a borylated GNR ($V_b = -300$ mV, $I = 30$ pA). (Right) Constant height current image of the marked rectangular region ($V_b = 2$ mV) using a CO-functionalized tip. (b) DFT simulation of the magnetization of a $(2B)_2$ -7AGNR. (c) Cotunneling current I vs. z through the ribbon in (a) suspended between tip and sample. (d) Normalized differential conductance of the suspended $(2B)_2$ -7AGNR as a function of V_b and z (see SI [11]). Two zero-bias resonances are observed. (e) Representative dI/dV spectra measured at the indicated z positions, with fits (dashed) using Frota functions [39]. (f) DFT relaxed structure of a suspended $(2B)_2$ -7AGNR. Constant spin-density isosurfaces are shown over the atomic structure; red arrows indicate the position of the B atoms. The inset shows the indicated region of the suspended GNR from a different angle.

antiparallel kinetic exchange [27]. A detailed analysis reveals that the hopping matrix elements between the two localized states at the sides of one 2B unit are very small ($t_{\text{intra}} \sim 18$ meV, see SI [11]). Consequently, the moiety formed by a 2B-doped ring surrounded by two Clar sextets is a very stable element that blocks conjugated electrons from hopping across. This explains the presence of a magnetic state because the borylated element acts as a barrier for valence band electrons of the 7AGNR segments [29], and induces spin polarized boundary states due to the non-trivial topology of this band [31]. Additionally, the 2B barrier also disconnects the boundary states at each side, and hinders the (anti-parallel) kinetic exchange between them. The stabilization of the triplet configuration is then the result of the weak direct overlap between both spin-polarized boundary states through the 2B barrier, which, due to the tiny hopping between them, dominates the exchange interaction and induces the ferromagnetic alignment of the spins according to Hund's rule.

We also studied GNRs with two consecutive 2B moieties like in Fig. 5(a,b), spaced by 1.2 nm. Transport experiments through these GNRs as a function of tip-sample distance (Fig. 5(c)) also reveal deviations from an exponential decay with z , but now showing two peak features at retraction distances $z_{p1} \approx 1.60$ nm and $z_{p2} \approx 3.05$ nm. These values are related to the positions of the 2B units (nominally ~ 2.0 and ~ 3.2 nm from the contact

point, respectively). A map of (normalized) differential conductance as a function of bias and z (Fig. 5(d)) shows that both current features are also caused by narrow zero-bias dI/dV resonances appearing at ranges $z < 1.9$ nm and 2.9 nm $< z < 3.5$ nm, respectively. Their line shape (Fig. 5(e)) is similar to the resonances observed for the single 2B case, and can also be attributed to Kondo states, which reflect the emergence of spin-polarization in the ribbon as each 2B unit is detached from the surface.

Although these results apparently suggest that each 2B behaves as an independent spin center, DFT simulations of free $(2B)_2$ -7AGNRs (Fig. 5(b)) find that the two singly-occupied boundary states between neighboring 2B elements interact strongly and open a large hybridization gap [30], forcing them into a closed shell configuration. As a consequence, the spin polarization vanishes between two 2B sites, but persists outside this region as two uncompensated spin 1/2 clouds (Fig. 5(b)) with barely no preferred relative spin alignment. From our electronic structure calculations [11, 30] we can characterize this hybridization by a relatively large effective hopping term t_{inter} between boundary states of neighboring 2B units, which contrasts with the weak hopping t_{intra} across each 2B unit. In fact, the electronic structure close to the Fermi level of a sequence of borylated units can be mapped onto the Su-Schrieffer-Heeger (SSH) model [45], characterized by two alternating hop-

pings along a 1D wire. Since $t_{\text{inter}} > t_{\text{intra}}$, an alternative way to understand the spin-polarized states in Fig. 5(b) is as zero-energy topological modes of a very short SSH chain. These simulations allows us to predict that a $S=1$ spin chain will emerge for larger inter-2B spacing, when both hopping terms become smaller than the Coulomb charging energy U of the boundary states [11].

To explore if inter-2B interactions survive in the experimental geometry, we simulated a $(2B)_2$ -7AGNR suspended between tip and sample. Fig. 5(f) show the spin polarization of a snapshot with one 2B moiety completely detached and the second partially bound to the surface. In contrast with the large spin cloud around the lifted single 2B in Fig. 4(c), here there is no spin density between the two 2B moieties, but a net $S=1/2$ cloud above, confirming the presence of interactions between 2B units. The second $S=1/2$ boundary cloud is expected to appear below the lower 2B only after the last boron atom is detached, being this responsible for the more extended Kondo effect observed in the experiment above z_{p2} . These results confirm the spin polarization predicted at the interface between $(2B)_2$ units and pristine 7AGNR segments [31], which in essence are zero-energy modes of the 7AGNR valence band of similar nature than those created by a single 2B unit at every side.

The peculiar spin polarization of single 2B units and dimers is a remarkable consequence of the large and long-range exchange interactions present in GNRs [7, 8, 31]. Our results support that spins survive in free-standing GNRs and can form $S = 1$ spin chains for low concentrations. Tuning the separation between 2B units is a promising strategy to control spin polarization through a change in the correspondence between inter-2B and intra-2B interactions. Furthermore, the stronger sensitivity of substitutional boron heteroatoms to chemical bonding endows these systems with ideal properties to manipulate complex spin states in chains.

We gratefully acknowledge financial support from Spanish AEI (MAT2016-78293-C6, FIS2017-83780-P, and the Maria de Maeztu Units of Excellence Programme MDM-2016-0618), from the European Union (EU) through Horizon 2020 (FET-Open project SPRING Grant. no. 863098), the Basque Departamento de Educación through the PhD fellowship No. PRE_2019_2.0218 (S.S.), the Xunta de Galicia (Centro singular de investigación de Galicia accreditation 2016-2019, ED431G/09), the University of the Basque Country (Grant IT1246-19), and the European Regional Development Fund (ERDF). I.P. also thanks Xunta de Galicia and European Union (European Social Fund, ESF) for the award of a predoctoral fellowship.

[†] Electronic address: daniel.sanchez@ehu.eus

[‡] Electronic address: ji.pascual@nanogune.eu

- [1] D. D. Awschalom, L. C. Bassett, A. S. Dzurak, E. L. Hu, and J. R. Petta, *Science* **339**, 1174 (2013).
- [2] M. Slota, A. Keerthi, W. K. Myers, E. Tretyakov, M. Baumgarten, A. Ardavan, H. Sadeghi, C. J. Lambert, A. Narita, K. Müllen, and L. Bogani, *Nature* **557**, 691 (2018).
- [3] F. Lombardi, A. Lodi, J. Ma, J. Liu, M. Slota, A. Narita, W. K. Myers, K. Müllen, X. Feng, and L. Bogani, *Science* **366**, 1107 (2019).
- [4] A. L. Sharpe, E. J. Fox, A. W. Barnard, J. Finney, K. Watanabe, T. Taniguchi, M. A. Kastner, and D. Goldhaber-Gordon, *Science* **365**, 605 (2019), arXiv:1901.03520 .
- [5] J. Cai, P. Ruffieux, R. Jaafar, M. Bieri, T. Braun, S. Blankenburg, M. Muoth, A. P. Seitsonen, M. Saleh, X. Feng, K. Müllen, and R. Fasel, *Nature* **466**, 470 (2010).
- [6] M. Corso, E. Carbonell-Sanromà, and D. G. de Oteyza, in *On-Surface Synthesis II* (Springer International Publishing, Cham, 2018) pp. 113–152.
- [7] J. Li, S. Sanz, M. Corso, D. J. Choi, D. Peña, T. Frederiksen, and J. I. Pascual, *Nat. Commun.* **10**, 200 (2019).
- [8] S. Mishra, D. Beyer, K. Eimre, S. Kezilebieke, R. Berger, O. Gröning, C. A. Pignedoli, K. Müllen, P. Liljeroth, P. Ruffieux, X. Feng, and R. Fasel, *Nat. Nanotechnol.* **15**, 22 (2020).
- [9] J. Li, S. Sanz, J. Castro-Esteban, M. Vilas-Varela, N. Friedrich, T. Frederiksen, D. Peña, and J. I. Pascual, *Phys. Rev. Lett.* **124**, 177201 (2020).
- [10] J. Lawrence, P. Brandimarte, A. Berdonces-Layunta, M. S. G. Mohammed, A. Grewal, C. C. Leon, D. Sanchez-Portal, and D. G. de Oteyza, *ACS Nano* **14**, 4499 (2020).
- [11] See Supplemental Material [url] for experimental and theoretical methods, and complementary measurements and simulations, which includes Refs. [12-22].
- [12] I. Horcas, R. Fernández, J. Gomez-Rodriguez, J. Colchero, J. Gómez-Herrero, and A. Baro, *Review of scientific instruments* **78**, 013705 (2007).
- [13] J. D. Hunter, *Computing in Science & Engineering* **9**, 90 (2007).
- [14] P. Kovsi, arXiv preprint arXiv:1509.03700 (2015).
- [15] E. Artacho, D. SánchezPortal, P. Ordejón, A. García, and J. M. Soler, *Phys. Stat. Solidi (b)* **215**, 809 (1999).
- [16] J. M. Soler, E. Artacho, J. D. Gale, A. García, J. Junquera, P. Ordejón, and D. Sánchez-Portal, *J. of Phys.: Cond. Matt.* **14**, 2745 (2002).
- [17] N. Troullier and J. L. Martins, *Phys. Rev. B* **43**, 1993 (1991).
- [18] S. García-Gil, A. García, N. Lorente, and P. Ordejón, *Phys. Rev. B* **79**, 075441 (2009).
- [19] M. Kolmer, P. Brandimarte, J. Lis, R. Zuzak, S. Godlewski, H. Kawai, A. Garcia-Lekue, N. Lorente, T. Frederiksen, C. Joachim, D. Sanchez-Portal, and M. Szymonski, *Nature Communications* **10** (2019), 10.1038/s41467-019-09315-6.
- [20] M. Dion, H. Rydberg, E. Schröder, D. C. Langreth, and B. I. Lundqvist, *Phys. Rev. Lett.* **92**, 599 (2004).
- [21] J. Klimeš, D. R. Bowler, and A. Michaelides, *J. Phys.: Condens. Matter* **22**, 022201 (2010).
- [22] N. Gonzalez-Lakunza, I. Fernández-Torrente, K. J. Franke, N. Lorente, A. Arnau, and J. I. Pascual, *Phys. Rev. Lett.* **100**, 156805 (2008).

* These two authors contributed equally to this work

- [23] X. Wang, G. Sun, P. Routh, D. H. Kim, W. Huang, and P. Chen, *Chem. Soc. Rev.* **43**, 7067 (2014).
- [24] P. Błoński, J. Tuček, Z. Sofer, V. Mazánek, M. Petr, M. Pumera, M. Otyepka, and R. Zboil, *J. Am. Chem. Soc.* **139**, 3171 (2017).
- [25] E. H. Lieb, *Phys. Rev. Lett.* **62**, 1201 (1989).
- [26] J. J. Palacios, J. Fernández-Rossier, and L. Brey, *Phys. Rev. B* **77**, 195428 (2008).
- [27] H. Gonzalez-Herrero, J. M. Gomez-Rodriguez, P. Mallet, M. Moaied, J. J. Palacios, C. Salgado, M. M. Ugeda, J.-Y. Veuillen, F. Yndurain, and I. Brihuega, *Science* **352**, 437 (2016).
- [28] M. Ijäs, M. Ervasti, A. Uppstu, P. Liljeroth, J. Van Der Lit, I. Swart, and A. Harju, *Phys. Rev. B* **88**, 075429 (2013), 1306.2723 .
- [29] E. Carbonell-Sanromà, P. Brandimarte, R. Balog, M. Corso, S. Kawai, A. Garcia-Lekue, S. Saito, S. Yamaguchi, E. Meyer, D. Sánchez-Portal, and J. I. Pascual, *Nano Lett.* **17**, 50 (2017).
- [30] E. Carbonell-Sanromà, A. Garcia-Lekue, M. Corso, G. Vasseur, P. Brandimarte, J. Lobo-Checa, D. G. De Oteyza, J. Li, S. Kawai, S. Saito, S. Yamaguchi, J. E. Ortega, D. Sánchez-Portal, and J. I. Pascual, *J. Phys. Chem. C* **122**, 16092 (2018), 1806.02385 .
- [31] T. Cao, F. Zhao, and S. G. Louie, *Phys. Rev. Lett.* **119**, 076401 (2017).
- [32] D. J. Rizzo, G. Veber, T. Cao, C. Bronner, T. Chen, F. Zhao, H. Rodriguez, S. G. Louie, M. F. Crommie, and F. R. Fischer, *Nature* **560**, 204 (2018), 1805.06470 .
- [33] O. Gröning, S. Wang, X. Yao, C. A. Pignedoli, G. Borin Barin, C. Daniels, A. Cupo, V. Meunier, X. Feng, A. Narita, K. Müllen, P. Ruffieux, and R. Fasel, *Nature* **560**, 209 (2018), 1805.06635 .
- [34] G. Kichin, C. Weiss, C. Wagner, F. S. Tautz, and R. Temirov, *J. Am. Chem. Soc.* **133**, 16847 (2011).
- [35] S. Kawai, S. Saito, S. Osumi, S. Yamaguchi, A. S. Foster, P. Spijker, and E. Meyer, *Nat. Commun.* **6**, 1 (2015).
- [36] R. R. Cloke, T. Marangoni, G. D. Nguyen, T. Joshi, D. J. Rizzo, C. Bronner, T. Cao, S. G. Louie, M. F. Crommie, and F. R. Fischer, *J. Am. Chem. Soc.* **137**, 8872 (2015).
- [37] Z. Pedramrazi, C. Chen, F. Zhao, T. Cao, G. D. Nguyen, A. A. Omrani, H.-z. Tsai, R. R. Cloke, T. Marangoni, D. J. Rizzo, T. Joshi, C. Bronner, W. Choi, F. R. Fischer, S. G. Louie, and M. F. Crommie, *Nano Lett.* **18**, 3550 (2018).
- [38] B. V. Senkovskiy, D. Y. Usachov, A. V. Fedorov, T. Marangoni, D. Haberer, C. Tresca, G. Profeta, V. Caciuc, S. Tsukamoto, N. Atodiresei, N. Ehlen, C. Chen, J. Avila, M. C. Asensio, A. Y. Varykhalov, A. Nefedov, C. Wöll, T. K. Kim, M. Hoesch, F. R. Fischer, and A. Grüneis, *ACS Nano* **12**, 7571 (2018).
- [39] H. O. Frota, *Phys. Rev. B* **45**, 1096 (1992).
- [40] M. Koch, F. Ample, C. Joachim, and L. Grill, *Nat. Nanotechnol.* **7**, 713 (2012).
- [41] J. Kondo, *Prog. Theor. Phys.* **32**, 37 (1964).
- [42] R. Temirov, A. Lassise, F. B. Anders, and F. S. Tautz, *Nanotechnology* **19**, 065401 (2008).
- [43] M. Ternes, A. J. Heinrich, and W.-D. Schneider, *J. Phys.: Condens. Matter* **21**, 053001 (2008).
- [44] M. Ternes, *New Journal of Physics* **17**, 063016 (2015).
- [45] W. P. Su, J. R. Schrieffer, and A. J. Heeger, *Phys. Rev. Lett.* **42**, 1698 (1979).

Magnetism of topological boundary states induced by boron substitution in graphene nanoribbons

Niklas Friedrich,^{1,*} Pedro Brandimarte,^{2,*} Jingcheng Li,¹ Shohei Saito,³ Shigehiro Yamaguchi,⁴ Iago Pozo,⁵ Diego Peña,⁵ Thomas Frederiksen,^{2,6} Aran Garcia-Lekue,^{2,6} Daniel Sánchez-Portal,^{2,7,†} and José Ignacio Pascual^{1,6,‡}

¹*CIC nanoGUNE, 20018 Donostia-San Sebastián, Spain*

²*Donostia International Physics Center (DIPC),
20018 Donostia-San Sebastián, Spain*

³*Graduate School of Science, Kyoto University, Kyoto 606-8502, Japan*

⁴*Graduate School of Science, Nagoya University, Nagoya 464-8602, Japan*

⁵*CiQUS, Centro Singular de Investigación en Química Biolóxica e Materiais Moleculares,
15705 Santiago de Compostela, Spain*

⁶*Ikerbasque, Basque Foundation for Science, Bilbao, Spain*

⁷*Centro de Física de Materiales CSIC-UPV/EHU,
20018 Donostia-San Sebastián, Spain*

(Dated: September 29, 2020)

Contents

I. Materials and Methods	2
A. Sample preparation	2
B. Lifting procedure	2
C. Normalization of differential conductance spectra	2
D. Presentation of experimental data	2
E. Details on ab-initio calculations	3
II. Supplementary Text	4
A. Lift of GNRs with 2B sites at different positions	4
B. Evolution of the Kondo resonance line width with retraction distances z	5
C. DFT simulations of the edge states and boron-induced inner states in 7AGNR	5
D. Electronic structure of 2B-7AGNR on lift-off configuration versus free standing	6
E. Minimal model of an isolated 2B center in 7AGNR	7
F. Electronic and magnetic interactions between neighbouring 2B centers	8

*These two authors contributed equally to this work

†Electronic address: daniel.sanchez@ehu.eus

‡Electronic address: ji.pascual@nanogune.eu

I. MATERIALS AND METHODS

A. Sample preparation

To prepare the Au(111) substrate we perform a cleaning cycle by sputtering the crystal with Neon ions for 10 minutes and afterwards annealing the crystal in UHV conditions ($p < 10^{-9}$ mbar) at $T = 740$ K for 15 minutes. We prepare our samples by simultaneously evaporating DBBA and B₂-DBTA molecular precursors on the clean Au(111) surface [? ? ?]. Afterwards an Ullmann reaction and cyclodhydrogenation are induced by successive annealing the sample to 200 °C for few minutes and flashing to 400 °C for 30 seconds.

The samples are prepared in situ and transferred directly into a homebuild STM kept with liquid Helium at ≈ 6 K. We use a PtIr tip with an atomically sharp gold termination. The tip is prepared by controlled indentation into the clean Au(111) surface.

B. Lifting procedure

The lifting is performed as following. After stabilization of the tip above the clean Au(111) surface with a fixed set of parameters ($I = 30$ pA, $V_b = -1000$ mV), we open the feedback loop of the control electronics. Afterwards, we position the tip above the termination of the GNR and approach towards the surface with a bias $V_b = 25$ mV. At some point during the approach a sudden increase in the current is observed. This corresponds to the formation of a tip-molecule bond and defines $z = 0$ during each experiment. After the tip-molecule bond is formed we are able to partially lift the GNR from the surface.

Custom cleaving trajectories are employed for the different molecules, depending on the strength of the tip-molecule bond. In the most robust cases we cleave the molecule by simple retraction along the z -axis. In less strongly bound cases, we need to move additionally in the xy -plane, following a trajectory along the direction of the GNR-backbone on the surface. However, we find that variations in the lifting trajectory do not influence at which z_1 we observe the peak in I and the Kondo-resonance in the differential conductance spectra.

C. Normalization of differential conductance spectra

Each individual spectrum taken at one z_0 was normalized following $G_{\text{norm}}(V, z_0) = \frac{G(V, z_0) - G_{\text{min}, z_0}}{G_{\text{max}, z_0} - G_{\text{min}, z_0}}$, where $G(V, z_0)$ is the measured dI/dV -signal at z_0 and G_{min, z_0} (G_{max, z_0}) is the minimal (maximal) value of $G(V, z_0)$ in the analysed bias interval. The normalization is only applied to the data presented in Fig. 4D.

D. Presentation of experimental data

The figures presenting experimental data were prepared using WSxM [?] and the python matplotlib library [?], perceptual continuous color scales for color maps are based on [?].

E. Details on ab-initio calculations

First-principles electronic structure calculations are performed using density functional theory as implemented in the SIESTA package [? ?], where the valence-electron wave functions are expanded using a linear combination of numerical atomic-orbitals as a basis set and the core electrons are replaced by norm-conserving Troullier-Martins pseudopotentials [?]. A double- ζ plus polarization (DZP) basis set is adopted for the surface Au atoms, where an extended basis is considered for the top atomic layer optimized for the description of the Au(111) surface [?]. The tip model is defined by a gold rod with its axis along the Au(100) crystalline direction and its valence-electrons described using a DZP basis set for s -orbitals and single- ζ non-polarized (SZ) basis for d -orbitals (i.e. DZP-SZd). Such geometry and basis set has been shown to provide a reasonable description of the contact, with a smooth local density of states at the tip apex around the Fermi level [?]. For the atoms defining the borylated ribbons a double- ζ non-polarized (DZ) basis set is employed, where the orbital radii are defined using a 30 meV energy shift [?]. Dispersive interactions between the borylated ribbon and the metallic surface are considered using the van der Waals density functional by Dion et al. [?] with the modified exchange by Klimeš, Bowler and Michaelides [?]. The real-space grid for integrations is defined using a 300 Ry energy cutoff [?]. The smearing of the electronic occupations is defined by an electronic temperature of 300 K with a Fermi-Dirac distribution. The self-consistency cycle is stopped when variations on the elements of the density matrix are lower than 10^{-5} as well as 10^{-5} eV for the Hamiltonian matrix elements.

The freestanding 2B-GNRs, as the one shown in Fig. 2A in the main text, are computed within a simulation cell that includes 20 and 40 Å of empty space in the directions along and perpendicular to the ribbon, respectively, to avoid interactions with the periodic replicas. Geometry optimizations are performed using the conjugate gradient (CG) method until all forces are lower than 20 meV/Å. For the calculations involving the suspended borylated GNRs, the Au(111) surface is represented by a 3-layer thick slab within a simulation cell of dimensions $46.16 \times 24.98 \text{ Å}^2$ along the periodic directions. A H passivation is employed at the reverse side of the slab in order to prevent spurious effects due to interaction between surface states belonging to the top and bottom surfaces of the slab [?]. A 1×2 k -point mesh is used to sample the bidimensional Brillouin zone. The slab defined in this way comprises 640 atoms (7680 orbitals), where the atoms from top Au layer are allowed to relax with the CG method until forces are lower than 20 meV/Å (the H passivation and the two bottom Au layers are kept fixed).

II. SUPPLEMENTARY TEXT

A. Lift of GNRs with 2B sites at different positions

In Fig. 1 we present two further examples of I - z retraction curves of two 2B-GNRs with the 2B site at 2.0 nm and 3.6 nm from the contact point, respectively. The peaks in the current are observed at $z_p = 1.2$ nm and $z_p = 2.4$ nm, in agreement with the different 2B to contact point distances. In both cases the peak in the current is caused by a zero-bias Kondo resonance, like in the case presented in the main text.

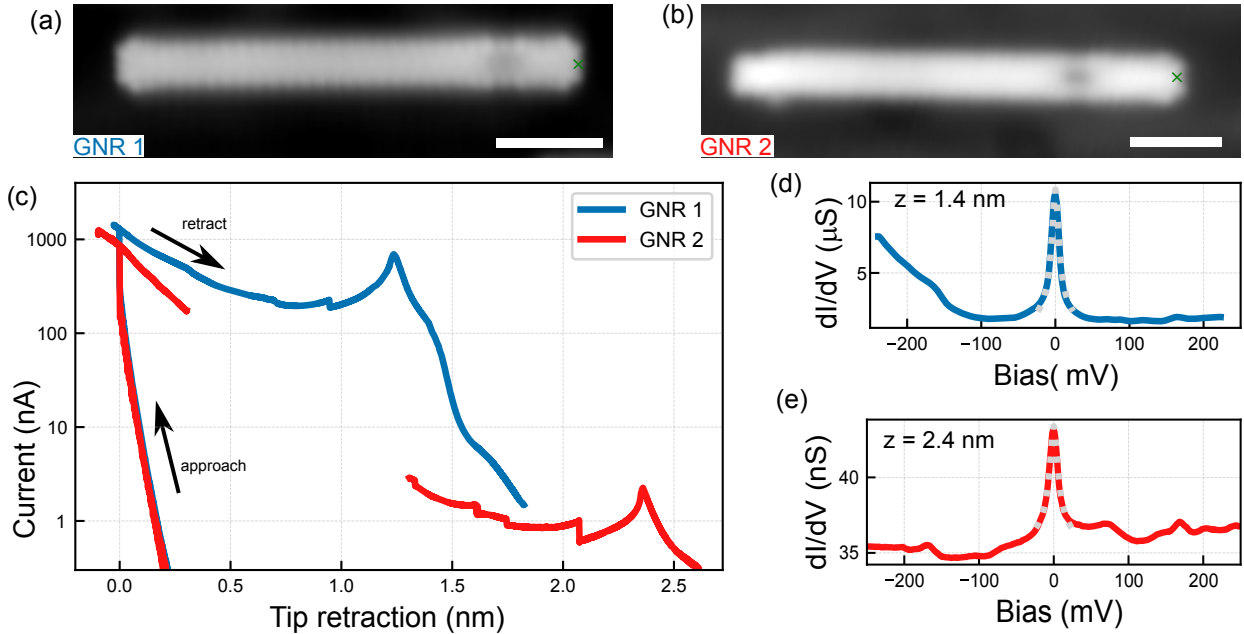


FIG. 1: **Fingerprint of magnetism in borilylated GNRs:** **A,B** STM constant current topography scan of two borilylated 7-AGNR ($V_b = -300$ mV, $I = 30$ pA) with the doping position at different distances from the lifting position. The green cross indicates the position from where the GNR is lifted. Scale bar is 3 nm. **C** Cotunnelling current I as a function of z for the GNRs depicted in **A** and **B**. The value of z at which the current peak is observed correlates with the position of the doping site in the ribbon. The lifting experiment is performed at $V_b = 25$ mV. **D,E** Spectrum over a larger bias window, taken at $z = 1.4$ nm ($z = 2.4$ nm) with GNR 1 (GNR 2) bridging tip and sample. The dotted grey lines are fitted Frota functions with $\text{HWHM} = 5.0 \pm 0.3$ mV (**D**, GNR 1) and $\text{HWHM} = 5.7 \pm 0.3$ mV (**E**, GNR 2).

B. Evolution of the Kondo resonance line width with retraction distances z

Figure 2 shows full width at half maximum (FWHM) and amplitude (A) of the Kondo resonances shown in Fig. 3 of the main manuscript. These are obtained by fitting a Frota function [?] plus an offset to the spectra. For $z \geq 2.92$ nm the Kondo resonance vanished and A dropped approximately by one order of magnitude. The Frota function was fitted to the data in the interval of $|V_b| < 20$ mV. We tested the stability of this procedure by increasing the size of the interval up to $|V_b| < 50$ mV. No qualitative changes and only minor quantitative changes of the FWHM were observed. A was unaffected by the interval's size.

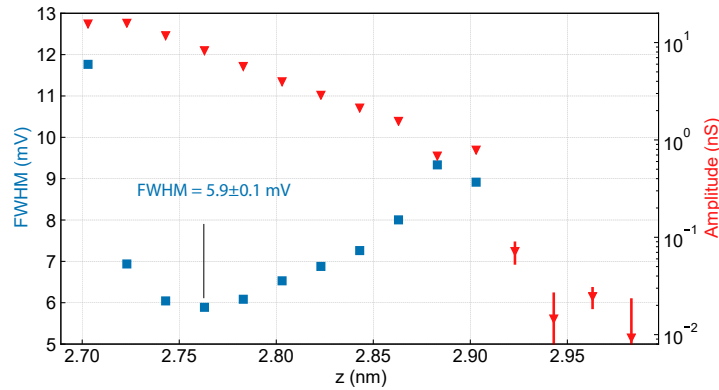


FIG. 2: **Frota lineshape as a function of z** : FWHM (left axis, blue squares) and amplitude (right axis, red triangles) obtained for the set of spectra in Fig. 3 of the main manuscript.

C. DFT simulations of the edge states and boron-induced inner states in 7AGNR

The boundary states induced by the substitutional boron pairs exhibit the same shape, symmetry, and decay towards the pristine segments as the 7AGNRs end states, localized in the zigzag terminations. Fig. 3 below presents a comparison between two 7AGNRs end states facing each other (shown in the top) and the 2B-induced bonding and anti-bonding states (bottom). Notice that, interestingly, for 2B centers the “bonding” state is higher in energy than the “anti-bonding” linear combination.

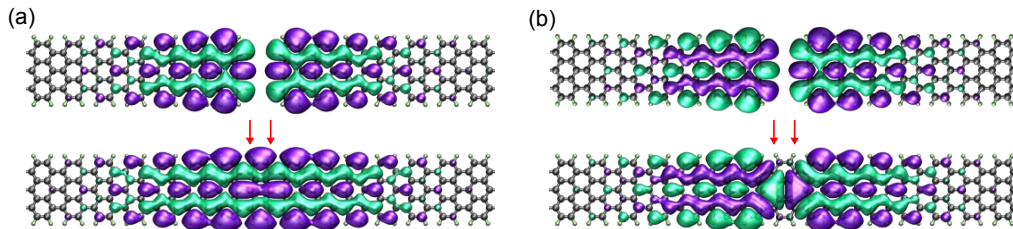


FIG. 3: **Wavefunction of edge states and 2B-induced states in 2B-7AGNRs**: Bonding (a) and anti-bonding (b) boundary states localized around the boron dimer (bottom) as compared to two 7AGNR edge states (top). Red arrows indicate the position of the boron atoms.

D. Electronic structure of 2B-7AGNR on lift-off configuration versus free standing

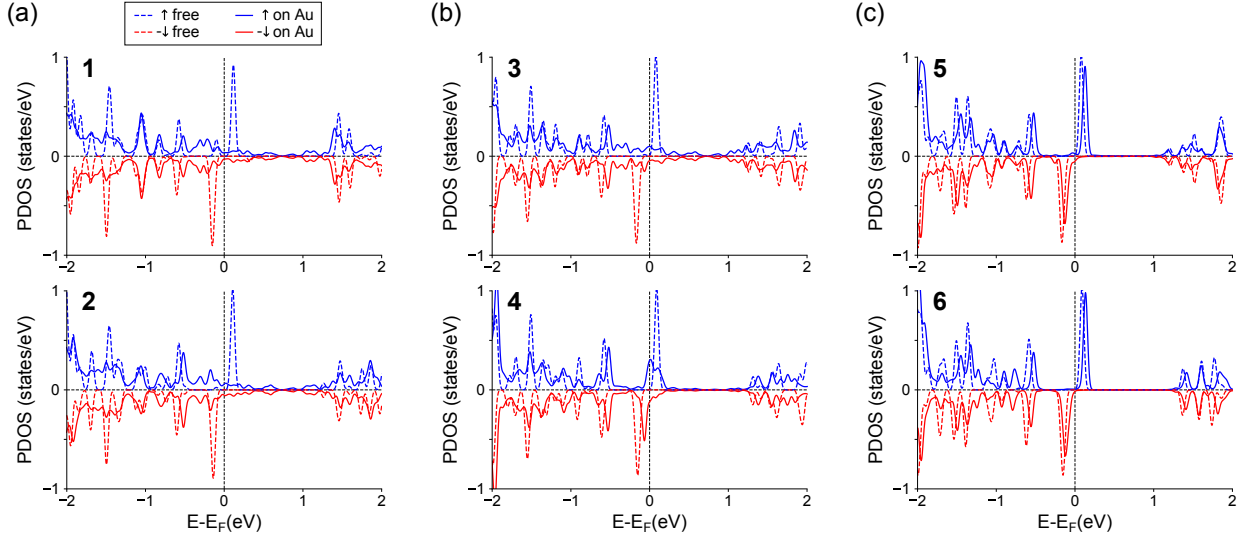


FIG. 4: Density of states projected on the C atoms within the boxed regions shown in Fig. 4 from the main text, here displayed in a larger energy window: solid lines are related to the configurations where a 2B-7AGNR is bridging a gold tip and a Au(111) surface (Fig. 4, main text), whereas the dashed lines are taken from a corresponding free standing 2B-7AGNR. Panels (a-c) corresponds to the three different configurations of Fig. 4 in the main text.

The density of states projected on the C atoms around each B atom (PDOS), inside the marked regions in Fig. 4 of the main text, are shown here in Fig. 4 for a wider energy window. Before detachment, when the B atoms are close to the Au substrate (regions **1**, **2**, and **3**), besides having the magnetism quenched, the hybridization with the substrate is reflected in the larger broadening of the PDOS at lower energies. This is in accordance with previously reported the results of fully borolated 7AGNR on Au(111) surface.[?] For the detached regions (**4**, **5**, and **6**), the intrinsic magnetism near the B atom is restored and the PDOS resemble the free standing ones (dashed lines). The small misalignment between the solid and dashed lines in these cases are due to the Fermi energy on the free standing 2B-7AGNR arbitrarily defined somewhere inside the gap.

E. Minimal model of an isolated 2B center in 7AGNR

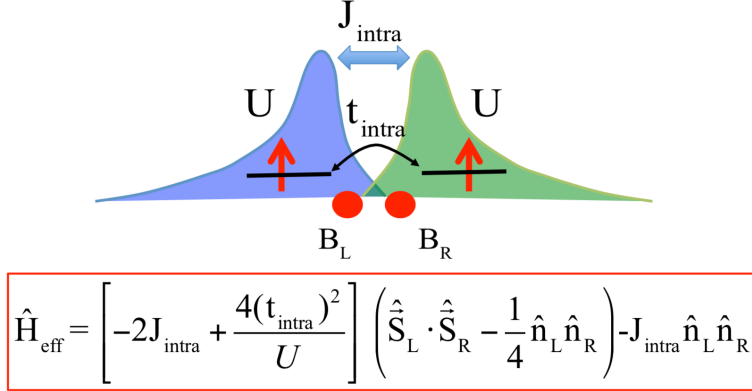


FIG. 5: **Minimal model of an isolated 2B center in a 7AGNR:** Two boundary states L and R, one at each side of the 2B pair and characterized by a charging energy U (Hubbard parameter), are connected by a hopping matrix element t_{intra} . We also add a Coulomb exchange interaction J_{intra} between electrons in different levels. The corresponding effective Hamiltonian, expressed in terms of spin $\hat{\mathbf{S}}$ and occupation \hat{n} operators at each site, is shown below in the relevant limit here, $U \gg t_{\text{intra}}$.

A single 2B moiety in a 7-armchair graphene nanoribbon (7AGNR) is found to build up a total spin $S=1$ due to the predominant ferromagnetic interaction between the two singly occupied boundary states (B-states) localized at each side. The purpose of this section is to formulate the minimal model (depicted in Fig. 5) capable of explaining the low-energy electronic structure and the magnetism of isolated 2B pairs.

The effective Hamiltonian describing an isolated 2B pair also can be seen in Fig. 5 in the limit $U \gg t_{\text{intra}}$. Exact and mean field solutions of this model are readily obtained and can be compared with the relative energies and the band structures of different DFT solutions. In particular, we use information from DFT simulations (both non-spin-polarized and spin-polarized with either ferromagnetic or anti-ferromagnetic spin alignment) to estimate the following values of the effective parameters describing the system according to the model of Fig. 5: the charging energy of each boundary state $U \sim 260$ meV, the effective hopping matrix element between both boundary states $t_{\text{intra}} \sim 18$ meV, and the Coulomb exchange interaction $J_{\text{intra}} \sim 17$ meV.

While the Coulomb exchange J_{intra} favours parallel alignment, the kinetic exchange (KE) term, given by $4(\frac{t_{\text{intra}}^2}{U})$ (Fig. 5) tends to align spins antiferromagnetically. The small value of t_{intra} relative to U translates into a small KE interaction, of the order of ~ 1.2 meV, i.e., around 14 times smaller than the Coulomb exchange within each 2B pair. Therefore, the ground state of an isolated 2B pair corresponds to a total spin $S=1$ as expected from Hund's rules.

F. Electronic and magnetic interactions between neighbouring 2B centers

We now consider the case of periodic doping of 7AGNRs with 2B centers. The distance between two 2B sites is given by the number n of 7AGNR unit cells defining the periodicity of the system. Fig. 6 compares the computed hopping matrix elements between B-states at each side of a given 2B pair (t_{intra}) and those between two neighbour 2B pairs (t_{inter}). These values are obtained by fitting to the Su-Schrieffer-Heeger (SSH) model [?] the B-derived in-gap states appearing in the non-spin-polarized DFT band structures in Fig. 5 of Ref.[?] for $2\text{B}-(7\text{AGNR})_n$ with $n = 3, \dots, 13$. The fitting is rather accurate for $n > 3$, while for $n=3$ there is a somewhat larger uncertainty due to the interaction between the lower B-derived state and the valence band of the 7AGNR near the Γ -point. As mentioned above we obtain a very small effective hopping parameter between the boundary states across the diboron

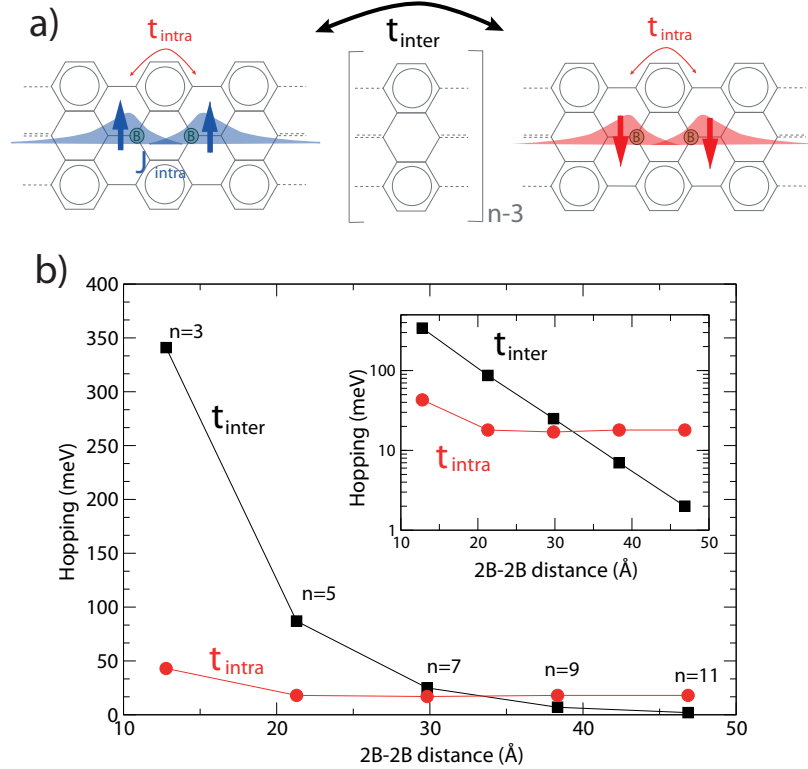


FIG. 6: **Electronic interactions between B-derived states from DFT calculations:** (a) Schematic model of a 2B-AGNR with intra-2B and inter-2B hopping terms indicated. J_{intra} represents the direct Coulomb exchange resulting in ferromagnetic alignment of the spins within each pair. (b) Computed values of intra-2B and inter-2B hopping terms from the analysis of non-spin-polarized DFT band structures of the periodic systems [?]. The inter-2B spacing given by n , the number of 7AGNR unit cells between 2B sites. The correspondence with the Su-Schrieffer-Heeger (SSH) model is evident. The inset shows the exponential decay of t_{inter} and magnifies the crossing point where the topology of the non-spin-polarized band structure of the system changes. However, as discussed in the text, the non-polarized solution is not relevant in the limit where $t_{\text{inter}} < U$ that clearly holds for $n \geq 5$.

moiety t_{intra} , which amounts to 18 meV for $n \geq 5$.

The effective electron hopping between proximal B states t_{inter} is much larger than t_{intra} for $n < 7$, and decreases exponentially with the separation, resulting residual above $n \geq 7$. The spacing between diboron sites in the results of Fig. 5 of the manuscript corresponds to $n = 3$. The inter-diboron hopping is very large in this case ($\sim 350 \text{ meV} > U$), resulting in a closed-shell state with no spin polarization in the spacing between them. The small electron hopping across a 2B site protects the outer B states, which maintain each a net spin polarization of $S=1/2$, as detected in Fig. 5.

The larger hopping between neighbour diboron sites than inside one, i.e., $t_{\text{inter}} > t_{\text{intra}}$, resemble a non-trivial bulk-boundary correspondence, as described by the SSH model. According to this model, for the smallest spacings between diborons ($n=3, 5$) boundary states are expected at the terminations since $t_{\text{intra}} < t_{\text{inter}}$. However, if we consider Coulomb correlations, only the case $n=3$ shows end states because it fulfills $U < t_{\text{inter}}$. The $n=5$ case, for which already $U > t_{\text{inter}}$, results in a chain with a spin texture formed by $S=1$ spins localized at the 2B sites and aligned antiferromagnetically along the chain due to the large kinetic exchange associated with t_{inter} .